



ARTICLE

<https://doi.org/10.1038/s41467-018-08041-9>

OPEN

The evolution of skyrmions in Ir/Fe/Co/Pt multilayers and their topological Hall signature

M. Raju ¹, A. Yagil², Anjan Soumyanarayanan ^{3,4}, Anthony K.C. Tan^{3,5}, A. Almoalem², Fusheng Ma¹, O.M. Auslaender² & C. Panagopoulos¹

The topological Hall effect (THE) is the Hall response to an emergent magnetic field, a manifestation of the skyrmion Berry-phase. As the magnitude of THE in magnetic multilayers is an open question, it is imperative to develop comprehensive understanding of skyrmions and other chiral textures, and their electrical fingerprint. Here, using Hall-transport and magnetic-imaging in a technologically viable multilayer film, we show that topological-Hall resistivity scales with the isolated-skyrmion density over a wide range of temperature and magnetic-field, confirming the impact of the skyrmion Berry-phase on electronic transport. While we establish qualitative agreement between the topological-Hall resistivity and the topological-charge density, our quantitative analysis shows much larger topological-Hall resistivity than the prevailing theory predicts for the observed skyrmion density. Our results are fundamental for the skyrmion-THE in multilayers, where interfacial interactions, multi-band transport and non-adiabatic effects play an important role, and for skyrmion applications relying on THE.

¹Division of Physics and Applied Physics, School of Physical and Mathematical Sciences, Nanyang Technological University, Singapore 637371, Singapore. ²Department of Physics, Technion, Haifa 32000, Israel. ³Data Storage Institute, Agency for Science, Technology and Research (A*STAR), 2 Fusionopolis Way, Singapore 138634, Singapore. ⁴Present address: Institute of Materials Research and Engineering, Agency for Science, Technology and Research, Singapore, Singapore. ⁵Present address: Cavendish Laboratory, University of Cambridge, JJ Thomson Avenue, Cambridge CB3 0HE, Cambridge, United Kingdom. These authors contributed equally: M. Raju, A. Yagil. Correspondence and requests for materials should be addressed to O.M.A. (email: ophir@physics.technion.ac.il) or to C.P. (email: christos@ntu.edu.sg)

Skyrmions are topologically protected, two-dimensional (2D), localized hedgehogs and whorls of spin¹. Originally invented as a concept in field theory for nuclear interactions², skyrmions are central to a wide range of phenomena in condensed matter^{3–5}. Their realization at room temperature (RT) in magnetic multilayers^{6–8} has generated considerable interest, fueled by technological prospects and the access granted to fundamental questions. The interaction of skyrmions with charge carriers^{1,8–12} gives rise to exotic electrodynamics, such as the topological Hall effect (THE)^{13,14}. The topological protection of skyrmions results from the quantization of their topological charge (Q_{sk}), which counts the number of times the magnetization unit-vector $\mathbf{n}(\mathbf{r})$ covers the unit-sphere. Q_{sk} is determined by $B_{\text{eff}}(\mathbf{r})$, the z -component of the emergent magnetic field that corresponds to the Berry phase accumulated by a spin tracking $\mathbf{n}(\mathbf{r})$ ^{1,15,16}.

$$Q_{\text{sk}} = \frac{1}{4\pi} \int d^2\mathbf{r} \mathbf{m} \cdot \partial_x \mathbf{n} \times \partial_y \mathbf{n} \equiv \frac{1}{\Phi_0} \int d^2\mathbf{r} B_{\text{eff}}(\mathbf{r}) = 0, \pm 1, \pm 2, \dots \quad (1)$$

Here $\Phi_0 = h/e$ is the flux quantum, h is Planck's constant, $-e$ is the electron charge. THE is the Hall response to $B_{\text{eff}}(\mathbf{r})$. When charge carriers flow through a conductor with their spins tracking the skyrmion spin texture, the topological-Hall resistivity (ρ_{TH}) is¹:

$$\rho_{\text{TH}} = PR'_0 n_{\text{T}} \Phi_0, \quad (2)$$

where n_{T} is the 2D density of total topological charge. Here R'_0 is an unknown Hall resistivity representing the effective density of charge contributing to THE. R'_0 is usually taken to be R_0 ^{13,17–19}, the ordinary Hall coefficient, which is extracted from the high field slope of the Hall resistivity (ρ_{yx}), and represents the total density of mobile charge. $0 < P < 1$ is the spin-polarization of the charge carriers, and $B_{\text{eff}}(\mathbf{r})$ is manifested through Φ_0 . Assuming skyrmions are the sole carriers of topological charge $|Q_{\text{sk}}| = 1$ implies $n_{\text{T}} = n_{\text{sk}}$, the density of isolated skyrmions. Thus, within the adiabatic approximation, one expects a straightforward correlation between ρ_{TH} and n_{sk} . From the first observations in B20 systems^{13,14} to the recent multilayers, THE has been used as an indicator for the presence of skyrmions^{8,17}. However, a clear understanding of the effect is still lacking²⁰, especially in technologically viable multilayer films^{8,18,19}, where disorder and interface effects can play an important role^{7,21,22}. In particular, and as we explain below, the THE features in these multilayers are subtle and call for careful analysis of the transport measurements, as we demonstrate in Supplementary Note 3 and Supplementary Note 4. In contrast, the situation in some B20 systems is straightforward as they show a distinguishable characteristic hump in ρ_{yx} as a function of applied magnetic field (H) and temperature (T), corresponding to a skyrmion lattice^{23,24}. However, even in B20 systems such a feature does not appear always²⁵. One of our main goals here is to elucidate the significance of the subtle features that characterize our multilayer and to test their relationship to skyrmions.

Using magnetic force microscopy (MFM) and transport measurements, we present a comprehensive picture of the evolution of magnetic textures and their THE signature in a multilayer film capable of hosting skyrmions from RT down to at least 5 K. We demonstrate the relationship between n_{sk} and $|\rho_{\text{TH}}|$ over a ≈ 200 K temperature range. As the applied field H is swept from saturation towards zero, we find that skyrmions aggregate in worm-like magnetic textures, which may carry large topological charge (Q_{W}), and manifest as peaks in ρ_{TH} . Quantitative modeling of these worm-textures uncovers qualitative agreement between

$\rho_{\text{TH}}(H, T)$ and $n_{\text{T}}(H, T)$. Despite this, we find a large quantitative discrepancy indicating that the effect in multilayers is more involved.

Results

Multilayer system. Here we use sputtered [Ir(1)/Fe(0.5)/Co(0.5)/Pt(1)]₂₀ (in parenthesis—thickness in nanometers; subscript denotes the number of repeats) multilayer films, with the composition chosen for exhibiting skyrmions across a large range of T . The RT characterization of the films indicates Dzyaloshinskii–Moriya interaction (DMI) $D \approx 2.0$ mJ/m², and exchange interaction $A \approx 11$ pJ/m⁸. The effective magnetic anisotropy (K_{eff}) varies in the range ≈ 0.2 – 0.01 MJ/m³ as we change T from 5 K to 300 K (Supplementary Note 2). As demonstrated here, control over n_{sk} through variation of T is the key for unambiguous identification of the skyrmion THE signature. Without this control, the correspondence between n_{sk} and the subtle THE signal, which we establish by direct imaging, is impossible to uncover. In contrast to the B20 compounds, which host lattices of tubular Bloch-skyrmions²⁶, multilayers sustain skyrmions with tunable properties, and offer smoother integration with existing spintronic technologies. Spin textures in multilayers are influenced by interlayer dipolar and exchange interactions, magnetic frustration²⁷, and granularity⁷, which can pin, stabilize, and deform the spin textures, and result in coupled pancake-skyrmions with different topologies^{22,27}. This complexity, and associated tunability, provide means for exploring the interplay between disorder, interactions, and topology.

Qualitative agreement between residual Hall signal and the magnetic textures. The magnetoresistance and Hall effect were measured using a lock-in with non-perturbative current densities ($\approx 10^5$ A/m²). The presence of skyrmions is associated with an additional component in the measured ρ_{yx} ^{13,14,17}. This contribution can be quantified by resolving ρ_{yx} into the ordinary (R_0H) and anomalous [$R_S M(H)$] Hall components^{13,17–19}, and ρ_{TH} :

$$\rho_{yx}(H) = R_0H + R_S M(H) + \rho_{\text{TH}}(H). \quad (3)$$

We estimate $\rho_{\text{TH}}(H)$ by $\Delta\rho_{yx}(H)$, the residual of the fit of $\rho_{yx}(H)$ to $\rho_{yx}^{\text{fit}}(H) = R_0H + R_S M(H)$, which also yields R_0 and R_S (Supplementary Figure 7). The accuracy of $\Delta\rho_{yx}$ is ensured by calibrating field offsets to avoid artifacts resulting from using different measurement setups (Supplementary Note 3 and Supplementary Figure 2). Our conservative estimate for the overall error in $\Delta\rho_{yx}$ including a contribution from data analysis, is ± 2 n Ω ·cm, corresponding to the non-zero residual signal beyond saturation, where there are no skyrmions. Figure 1a shows $\Delta\rho_{yx}(H)$ at 5 K, with the overall features persisting to at least 300 K⁸.

The features of $\Delta\rho_{yx}(H)$ in Fig. 1a are subtle. Here, we use MFM to determine the correspondence of these features with the magnetic texture. For this we followed the same field sweep from saturation as we did for $\Delta\rho_{yx}(H)$ and magnetization [$M(H)$]⁸—the images were acquired at field increments as H was swept (Supplementary Note 1). Figure 1b–k shows the result for 5 K. Overall, we observe a similar evolution of the magnetic textures at $T = 50, 100, 150, 200$ K (Supplementary Figures 17 to 20).

We begin by comparing the magnetic textures to $\Delta\rho_{yx}(H)$. Beyond saturation, MFM shows the null signal expected for a polarized ferromagnet [Supplementary Figure 16(a)]. This is accompanied by the suppression of $\Delta\rho_{yx}$ (Fig. 1a) as expected for the topologically trivial polarized state. The onset of $\Delta\rho_{yx}$ commences at $\mu_0H \approx -0.3$ T with the nucleation of sub-100 nm magnetic domains (Fig. 1b), which we identify as Néel-skyrmions²¹. By $\mu_0H \approx -0.25$ T (Fig. 1c) the increasing n_{sk}

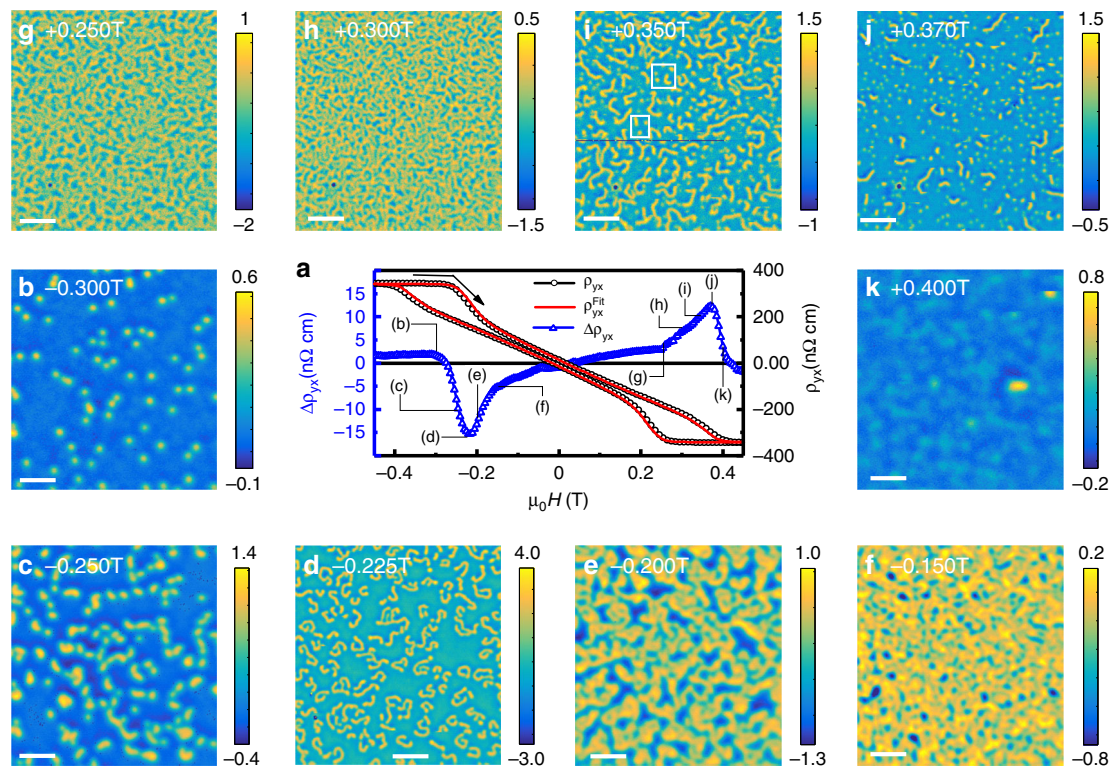


Fig. 1 Evolution of magnetic textures and THE with H at $T = 5$ K. **a** $\rho_{yx}(H)$, $\rho_{yx}^{fit}(H)$, and the residual $\Delta\rho_{yx}(H) = \rho_{yx}(H) - \rho_{yx}^{fit}(H) \approx \rho_{TH}(H)$. The black arrow indicates the field sweep direction for $\Delta\rho_{yx}$ and MFM, while ρ_{yx} and ρ_{yx}^{fit} are shown for both sweep directions. **b–k** Selected MFM scans [full sequence in Supplementary Figure 16, scan-height $h = 75, 60, 40, 60, 65, 50, 60, 50, 45, 60$ nm for each of **b–k**; color bars give the range of Δf , scale bars are $1 \mu\text{m}$]. Frames in (i) mark features in focus in Fig. 3b–g

corresponds to a substantial $\Delta\rho_{yx}$ as expected from $|\rho_{TH}| \propto n_{sk}^1$. Also, as n_{sk} increases, skyrmions aggregate to form worm-like features (Fig. 1c). By $\mu_0 H \approx -0.225$ T, images show only worms (Fig. 1d, e). Surprisingly, at this field $\Delta\rho_{yx}$ peaks, suggesting a significant contribution from the worms which may have nontrivial topology. Meanwhile, the dense textures at intermediate H (Fig. 1f–h, and Supplementary Figures 17 and 18) correspond to reduced, yet finite, $\Delta\rho_{yx}$. Careful inspection of such scans reveals worm-like features, to which we attribute the finite magnitude of $\Delta\rho_{yx}$ (Supplementary Note 7).

As $H = 0$ is approached, the worms evolve into labyrinthine helical stripes, and proliferate at the expense of the polarized background. This is coincident with the suppression of $\Delta\rho_{yx}$, highlighting the close relationship between $\Delta\rho_{yx}$ and the magnetic texture. As H is increased towards positive saturation, the labyrinthine stripes evolve into worms, skyrmions, and eventually a uniformly polarized phase (Fig. 1i–k). For a texture with an opposite topological charge, the sign of $\Delta\rho_{yx}$ is reversed when $H > 0$. However, the MFM contrast does not change, due to the reversal of the tip magnetization near 0.1 T.

The distinct field ranges for isolated skyrmions (near saturation), worms (negative peak in $\Delta\rho_{yx}$), and their coexistence (positive peak in $\Delta\rho_{yx}$) (cf. Supplementary Note 6), offer a unique opportunity to compare the magnetic texture with $\Delta\rho_{yx}$. In particular: (i) Does $\Delta\rho_{yx}$ track n_{sk} ? (ii) How do worms produce such a large $\Delta\rho_{yx}$? (iii) Is there quantitative consistency between $\Delta\rho_{yx}$ and n_T ?

To address (i) we exploit $n_{sk}(T)$, which increases by an order-of-magnitude when we increase T from 5 to 200 K (Fig. 2). We attribute this proliferation to the suppression of K_{eff} with temperature⁸. Interestingly, skyrmion size is only weakly T -dependent and does not change significantly within our

resolution, not unlike theoretical predictions²⁸. However, further experiments with similar imaging conditions are required to confirm the size variation. Importantly, we find that $\Delta\rho_{yx}(T)$ tracks $n_{sk}(T)$ over the entire range (Fig. 2a), and gives $\approx 0.6 \text{ n}\Omega \cdot \text{cm}$ per skyrmion/ μm^2 . This correlation between skyrmion nucleation and the emergence of $\Delta\rho_{yx}$ strongly points towards the topological origin of the residual signal.

Magnetic worms and their topological charge. Having established the direct correspondence between n_{sk} and $\Delta\rho_{yx}$, we now examine the worms. Though the presence of worms is expected in systems with competing interactions, such as in ferromagnetic films²⁹, their topological role is not obvious. In early MFM work on Bloch skyrmions in a B20 compound²⁶, helical stripe domains resulting from merging skyrmions were described by two half-skyrmions connected by a topologically trivial straight domain²⁶, and hence a topological charge of $Q_w = \pm 1$. This motivates us to examine whether worms carrying a topological charge given by $Q_{sk} = \pm 1$ can describe our results. We therefore plot $n_{sk} + n_w$ (n_w is the number of worms per unit area) in Fig. 3a, with the sign chosen from the sign of $\Delta\rho_{yx}$. As the plot shows, both $n_{sk}(H)$ and $n_{sk}(H) + n_w(H)$ do not track $\Delta\rho_{yx}(H)$. This calls for a closer look at the topological nature of the worms.

The following analysis of the topological charge of worms is motivated by sequences like Fig. 1b–d [also in Supplementary Figures 17(n)–(o)], which suggest that worms result from skyrmions clustering as n_{sk} increases. The transition of worms into typical stripe domains with $|Q_w| = 1$ requires a complete unwinding of their internal spin structure. The energy barrier for this suggests that the effective topological charge should be at least equal to the total number of skyrmions that form a worm

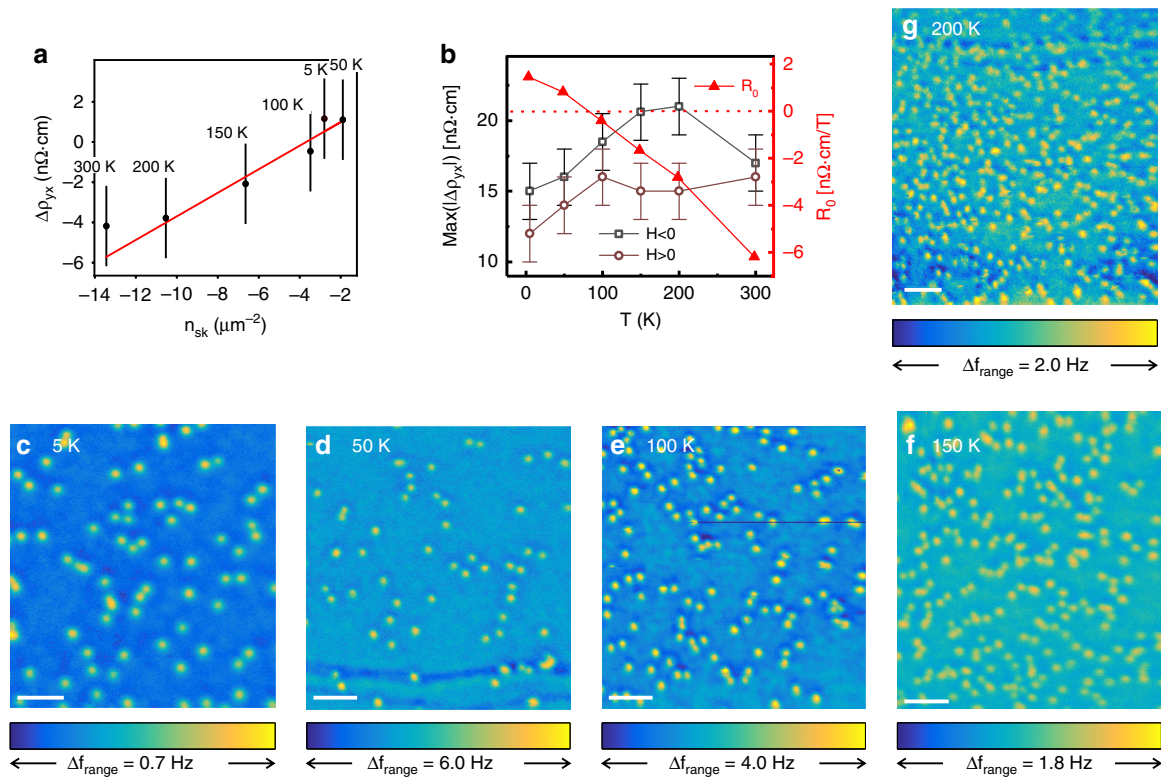


Fig. 2 Temperature dependence of n_{sk} , $\Delta\rho_{yx}$, and R_0 . The sign of n_{sk} is chosen to match $\Delta\rho_{yx}$. **a** $\Delta\rho_{yx}$ as a function of n_{sk} for different temperatures at $\mu_0 H = -0.3T$. Labels show the measurement temperature. Error-bars for $\Delta\rho_{yx}$ represent a conservative estimate of the systematic error. Errors for n_{sk} are smaller than the symbols. The line is a linear fit (slope $0.6 \pm 0.1 \text{ n}\Omega \cdot \text{cm}/\mu\text{m}^{-2}$, intercept $2.2 \pm 0.8 \text{ n}\Omega \cdot \text{cm}$). **b** Left axis: magnitude of the THE peaks ($H < 0$ —squares, $H > 0$ —circles). Right axis: the fit parameter $R_0(T)$ from Eq. (3) (triangles). **c–g** MFM scans showing isolated skyrmions for $n_{sk}(T)$ in **a**. [**c–g** scan-height $h = 75, 40, 40, 100, 40 \text{ nm}$, (**c**) is Fig. 1b, scale bars are $1 \mu\text{m}$]

(i.e., $|Q_w| > 1$). While skyrmions are expected to repel each other on very short length-scales because of exchange coupling³⁰, clusters can be stabilized by attraction on an intermediate scale, due to exchange frustration³¹.

Here our recent work, a magnetic multipole expansion of the field from skyrmions (MEFS)²¹, provides a direct method to associate an effective Q_w with each worm. Figure 3b–g shows two typical examples where we fit the measured signal from worms by trains of skyrmions. Such images, which contain both skyrmions and worms, provide the foundation for this kind of analysis—the isolated skyrmions serve to constrain the fit amplitude per skyrmion, and improve the accuracy (Supplementary Note 7). Meanwhile, the analysis of images containing only worms (Fig. 1d) hinges on skyrmions–skyrmion repulsion on a length scale comparable to their radius³⁰. Therefore, the number of skyrmions clustered in a worm is determined by the total length of the worm, and the typical radius of skyrmions ($\approx 40 \text{ nm}$ ²¹). For images with densely packed features (e.g., Fig. 1f–h) identifying and extracting the worms themselves requires additional image processing, for which we employ a deep-learning-model-based algorithm that extracts features relevant for classification from supplied examples (Supplementary Note 7). We note however, that while this analysis provides additional evidence for the correlation between magnetic textures and the $\Delta\rho_{yx}$ that we extract, our main conclusion does not rely on it. In all cases, our analysis allows us to compute the total $n_T(H)$ from $\Sigma Q_w + \Sigma Q_{sk}$, where ΣQ_w is the topological charge of a worm after assigning an appropriate number of skyrmions to it, and we assume that all skyrmions (including those in worms) have $Q_{sk} = \pm 1$, with the sign chosen to match the sign of $\Delta\rho_{yx}$.

To further verify our assertion of worms as trains of skyrmions, we have performed basic simulations of magnetization and the resulting evolution of magnetic textures in our multilayer stack. Simulations were performed using the MuMax³ package³² at $T = 0 \text{ K}$ for two different sets of magnetic parameters relevant to the magnetization of the stacks at different temperatures. In the simulations the field is swept incrementally towards saturation from $H = 0$. The magnetic texture in the simulations starts from labyrinthine stripes and evolves into worms, skyrmions and eventually a fully polarized state, in agreement with our experimental results. A complete set of simulated MFM images is shown in Supplementary Figures 10 and 11.

Figure 4 shows representative simulated maps of $n_z(\mathbf{r})$, the corresponding MFM images, and the contribution to Q_{sk} from each individual domain. Dashed domains in Fig. 4c, f mark skyrmion trains which appear as worms in the MFM scans (Fig. 4b, e), clearly indicating $|Q_w| > 1$. Here, we point out that while these results are in qualitative agreement with the experimental evolution of magnetic textures and the formation of worms, the simulations do not account for disorder and thermal effects in the multilayers. Addition of such effects and a full theoretical treatment is necessary for a deeper understanding of skyrmion trains and skyrmion–skyrmion interactions.

The qualitative match between $n_T(H)$ and $\Delta\rho_{yx}(H)$ (Fig. 3a), and the formation of worms from the clustering of skyrmions, as suggested by our micromagnetic simulations, reinforces our modeling of worms as trains of skyrmions. These results provide additional evidence that $\Delta\rho_{yx}$ results from skyrmion textures and is thus topological in nature, indicating $\Delta\rho_{yx} \approx \rho_{TH}$. Our observations on the emergence of worms with a potentially high

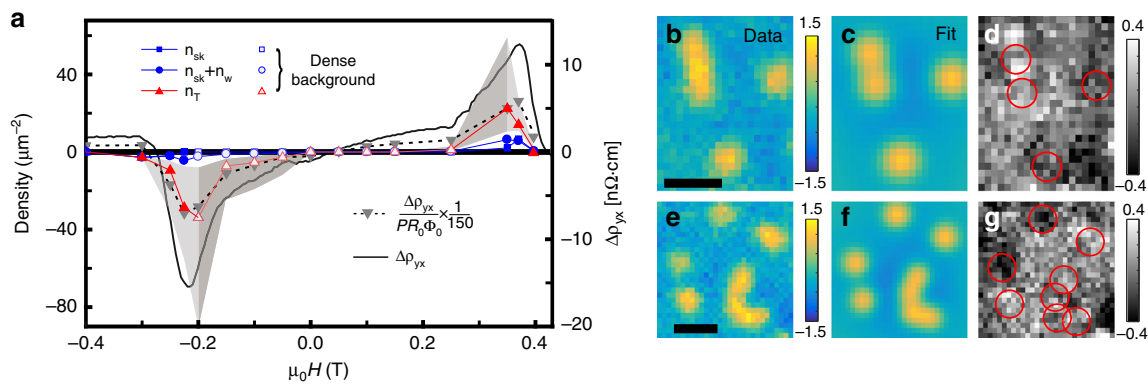


Fig. 3 Comparison between $\Delta\rho_{yx}$ and the signed density of topological charge at 5 K. **a** Right axis: $\Delta\rho_{yx}$ (solid line). Left axis: n_{sk} (squares), $n_{sk} + n_w$ (circles), n_T (triangles), and $\Delta\rho_{yx}/(PR_0\Phi_0)$ (cf. Eq. (2), inverted triangles with dotted line) using $P = 0.56^{43}$ and R_0 from Fig. 2b. For n_T , each worm is assigned several skyrmions $|Q_w|$ by fit, and each isolated skyrmion is counted once. Empty symbols indicate points with a lower confidence, that result from counting worms in a dense background (Supplementary Note 7). Shaded area shows confidence bounds for n_T resulting from fit details (Supplementary Note 7). **b, e** Zooms on areas in Fig. 1i with skyrmions and isolated worms. **c, f** Results of MEFS fits wherein all skyrmions, including those assigned to worms, are treated as identical. The fit peak height ≈ 1.15 Hz, full width at half maximum (FWHM) ≈ 100 nm, and $|Q_w| = 2$ in **(c)** and $|Q_w| = 4$ in **f**. **d, g** Difference plots between **b** and **c**, and between **e** and **f**, showing the quality of the fit. Circles give the locations of the skyrmions in the fit. [The scale bars in **b** and **e** are 200 nm]

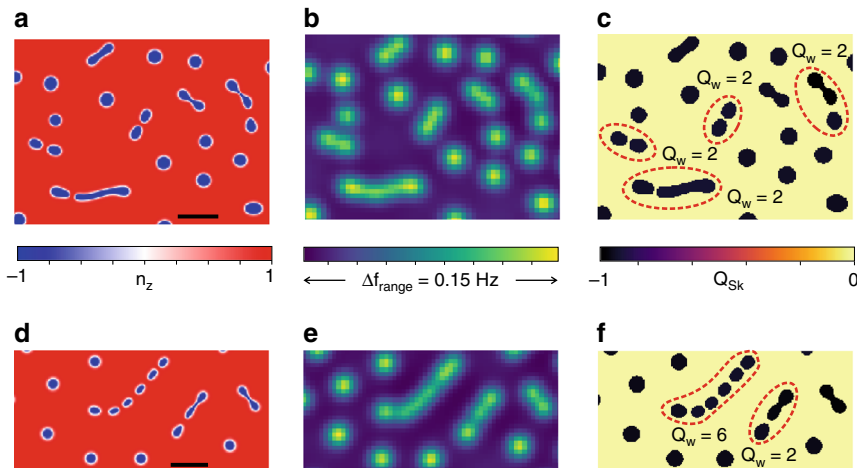


Fig. 4 Micromagnetic simulations of magnetic textures (Supplementary Note 5) for two sets of magnetic parameters corresponding to 5 and 200 K: **a–c** $A = 11$ pJ/m, $D = 2$ mJ/m², $M_s = 1.34$ MA/m, $K_{eff} = 0.2$ MJ/m³, and **d–f** $A = 11$ pJ/m, $D = 2$ mJ/m², $M_s = 1.16$ MA/m, $K_{eff} = 0.05$ MJ/m³. **a, d** 2D maps of the out-of-plane magnetization (n_z) at 0.230 T. **b, e** Simulated MFM images at $h = 40$ nm obtained by integrating the stray field from the micromagnetic simulations and convolving with a model for the tip (Supplementary Note 5). **c, f** Contribution to the topological charge from each domain, calculated using Eq. (1) (Supplementary Note 5). Dashed lines highlight trains of skyrmions which appear as individual worms in the MFM scans. [The scale bars in **a** and **d** are 200 nm]

topological number, previously not noticed experimentally, indicate they are distinct from trivial spin spirals, and form an essential part of the phase diagram for multilayer skyrmions³³. The presence of worms in a tunable multilayer offers a platform for studying skyrmion–skyrmion interactions over a wide parameter range, as well as applications, such as skyrmion racetracks⁷.

Quantitative agreement between transport and imaging. Having explored the nontrivial topology of the worms and a qualitative match between $\rho_{TH}(H, T)$ and $n_T(H, T)$, we examine the quantitative match. As we show in Fig. 3a, the density of topological charge estimated from THE [$\Delta\rho_{yx}/(PR_0\Phi_0)$, Eq. (2)] indicates a two-orders-of-magnitude discrepancy. This implies that simply using Eq. (2) with $R'_0 = R_0$ to understand the topological signatures of chiral magnetic textures in multilayer

skyrmion-hosts does not yield a comprehensive description of the measured $\Delta\rho_{yx}$.

A possible culprit is the assignment $R'_0 = R_0$ in Eq. (2)³⁴, which is justified for a single band material. This is not the case here: Bulk Fe and Co, the ferromagnetic ingredients of our multilayer stack, have several active electron and hole bands³⁵. In such materials R_0 is suppressed because electrons and holes, which experience the same H , compensate each other's contributions. The cancellation estimated from values reported for bulk Fe³⁵ indicate suppression of R_0 by an order of magnitude from the separate contributions of individual bands, partially addressing the discrepancy (Supplementary Note 8). Importantly, the cancellation may not happen in the same way for B_{eff} —the Berry-phase can act differently on charge carriers from different bands²³, with an associated sensitivity to occupation³⁶. The fact that the peak value of $\Delta\rho_{yx}(H)$ changes by only $\approx 25\%$ with T despite the sign change of $R_0(T)$ (Fig. 2b), probably because of

small variations of the occupations of the compensating bands, further confirms that $R_0 \neq R_0$. In this case, using R_0 in Eq. (2) underestimates ρ_{TH} ^{18,19}, although once R_0 is determined this fundamental equation may still be used. For this it is essential to account for the electronic band structure of the chiral magnet.

Finally, we comment on the nature of spin transport in multilayers. Here, transport is influenced by various length scales such as the thickness of individual layers, their mean free path (l), charge and spin conductivities, spin diffusion length (l_s), and the size of the magnetic textures—including the domain walls and their chirality. In our case, the radius of the skyrmions is ≈ 40 nm and the domain wall width ≈ 7 – 14 nm ($\sqrt{A/K_{\text{eff}}}$), where, $A \approx 11$ pJ/m and ≈ 0.2 – 0.05 MJ/m³. These length scales are comparable to the transport length scales reported for single thin layers ($l_{\text{Co}} \approx 5$ nm and $l_{\text{Pt}} \approx 13$ nm, $l_{s-\text{Pt}} \approx 1$ – 10 nm)³⁷, indicating their relevance to the relationship between ρ_{TH} and n_{sk} . Spin scattering from interfaces and magnetic textures such as domain walls may cause spin-flip scattering, resulting in a non-adiabatic, spin independent transport^{38–40}. As a result of the disordered skyrmion configurations, the charge carriers experience an inhomogeneous emergent field, in contrast to charge carriers in bulk systems which experience a systematically varying uniform emergent field due to the ordered arrangement of skyrmion textures. Notably, spin scattering in multilayer systems and its contribution to the anomalous Hall effect is dominated by skew scattering⁴¹. Hence, a better understanding of this contribution may help resolve the discrepancy between the observed and the expected THE signal^{38–40,42}.

Discussion

Our complementary imaging and electrical transport studies provide clear evidence for the correlation between $\Delta\rho_{yx}$ and the topology of the magnetic texture in technologically viable magnetic multilayers. Furthermore, we elucidate the complexity of the Berry-phase associated with the electrical fingerprint of chiral magnetic textures in those skyrmions hosting platforms. For a comprehensive understanding and in order to utilize THE emerging from magnetic skyrmions, it is imperative to consider (a) the band structure contributing to THE, (b) the possibility of $|Q_{\text{sk}}| > 1$ ²⁷ and skyrmion–skyrmion interactions³¹, (c) the coupling of skyrmions across layers and complex magnetic textures in buried interfaces²², (d) the contribution from topologically trivial chiral configurations driven by magnetic spin-frustration²⁰, and (e) the validity of the commonly assumed adiabatic approximation²⁰.

Data availability

The authors declare that the data supporting the findings of this study are available within the paper, and its Supplementary Information.

Received: 4 March 2018 Accepted: 6 December 2018

Published online: 06 March 2019

References

- Nagaosa, N. & Tokura, Y. Topological properties and dynamics of magnetic skyrmions. *Nat. Nanotechnol.* **8**, 899–911 (2013).
- Skyrme, T. H. R. A non-linear field theory. *Proc. R. Soc. Lond. A* **260**, 127–138 (1961).
- Sondhi, S. L., Karlhede, A., Kivelson, S. A. & Rezayi, E. H. Skyrmions and the crossover from the integer to fractional quantum Hall effect at small Zeeman energies. *Phys. Rev. B* **47**, 16419–16426 (1993).
- Senthil, T., Vishwanath, A., Balents, L., Sachdev, S. & Fisher, M. P. A. Deconfined quantum critical points. *Science* **303**, 1490–1494 (2004).
- Wang, F., Kivelson, S. A. & Lee, D.-H. Nematicity and quantum paramagnetism in FeSe. *Nat. Phys.* **11**, 959–963 (2015).
- Moreau-Luchaire, C. et al. Additive interfacial chiral interaction in multilayers for stabilization of small individual skyrmions at room temperature. *Nat. Nanotechnol.* **11**, 444–448 (2016).
- Woo, S. et al. Observation of room-temperature magnetic skyrmions and their current-driven dynamics in ultrathin metallic ferromagnets. *Nat. Mater.* **15**, 501–506 (2016).
- Soumyanarayanan, A. et al. Tunable room-temperature magnetic skyrmions in Ir/Fe/Co/Pt multilayers. *Nat. Mater.* **16**, 898–904 (2017).
- Bogdanov, A. N. & Rößler, U. K. Chiral symmetry breaking in magnetic thin films and multilayers. *Phys. Rev. Lett.* **87**, 037203 (2001).
- Soumyanarayanan, A., Reyren, N., Fert, A. & Panagopoulos, C. Emergent phenomena induced by spin–orbit coupling at surfaces and interfaces. *Nature* **539**, 509–517 (2016).
- Jiang, W. et al. Direct observation of the skyrmion Hall effect. *Nat. Phys.* **13**, 162–169 (2016).
- Litzius, K. et al. Skyrmion Hall effect revealed by direct time-resolved X-ray microscopy. *Nat. Phys.* **13**, 170–175 (2017).
- Neubauer, A. et al. Topological Hall effect in the A phase of MnSi. *Phys. Rev. Lett.* **102**, 186602 (2009). Erratum *Phys. Rev. Lett.* **110**, 209902 (2013).
- Lee, M., Kang, W., Onose, Y., Tokura, Y. & Ong, N. P. Unusual Hall effect anomaly in MnSi under pressure. *Phys. Rev. Lett.* **102**, 186601 (2009).
- Ye, J. et al. Berry phase theory of the anomalous Hall effect: application to colossal magnetoresistance manganites. *Phys. Rev. Lett.* **83**, 3737–3740 (1999).
- Bruno, P., Dugaev, V. K. & Taillefer, M. Topological Hall effect and Berry phase in magnetic nanostructures. *Phys. Rev. Lett.* **93**, 096806 (2004).
- Matsumo, J. et al. Interface-driven topological Hall effect in SrRuO₃–SrIrO₃ bilayer. *Sci. Adv.* **2**, e1600304 (2016).
- Maccariello, D. et al. Electrical detection of single magnetic skyrmions in metallic multilayers at room temperature. *Nat. Nanotechnol.* **13**, 233–237 (2018).
- Zeissler, K. et al. Discrete Hall resistivity contribution from Néel skyrmions in multilayer nanodiscs. *Nat. Nanotechnol.* <https://doi.org/10.1038/s41565-018-0268-y> (2018).
- Denisov, K. S., Rozhansky, I. V., Averkiev, N. S. & Lähderanta, E. A nontrivial crossover in topological Hall effect regimes. *Sci. Rep.* **7**, 17204 (2017).
- Yagil, A. et al. Stray field signatures of Néel textured skyrmions in Ir/Fe/Co/Pt multilayer films. *Appl. Phys. Lett.* **112**, 192403 (2018).
- Legrand, W. et al. Hybrid chiral domain walls and skyrmions in magnetic multilayers. *Sci. Adv.* **4**, eaat0415 (2018).
- Ritz, R. et al. Giant generic topological Hall resistivity of MnSi under pressure. *Phys. Rev. B* **87**, 134424 (2013).
- Kanazawa, N. et al. Discretized topological Hall effect emerging from skyrmions in constricted geometry. *Phys. Rev. B* **91**, 041122 (2015).
- Spencer, C. S. et al. Helical magnetic structure and the anomalous and topological Hall effects in epitaxial B20 Fe_{1–x}Co_xGe films. *Phys. Rev. B* **97**, 214406 (2018).
- Milde, P. et al. Unwinding of a skyrmion lattice by magnetic monopoles. *Science* **340**, 1076–1080 (2013).
- Rózsa, L. et al. Formation and stability of metastable skyrmionic spin structures with various topologies in an ultrathin film. *Phys. Rev. B* **95**, 094423 (2017).
- Tomasello, R. et al. Origin of temperature and field dependence of magnetic skyrmion size in ultrathin nanodots. *Phys. Rev. B* **97**, 060402 (2018).
- Seul, M. & Andelman, D. Domain shapes and patterns: the phenomenology of modulated phases. *Science* **267**, 476–483 (1995).
- Lin, S.-Z., Reichhardt, C., Batista, D. & Saxena, A. Particle model for skyrmions in metallic chiral magnets: dynamics, pinning, and creep. *Phys. Rev. B* **87**, 214419 (2013).
- Rózsa, L. et al. Skyrmions with attractive interactions in an ultrathin magnetic film. *Phys. Rev. Lett.* **117**, 157205 (2016).
- Vansteenkiste, A. et al. The design and verification of mumax3. *AIP Adv.* **4**, 107133 (2014).
- Dupé, B., Hoffmann, M., Paillard, C. & Heinze, S. Tailoring magnetic skyrmions in ultra-thin transition metal films. *Nat. Commun.* **5**, 4030 (2014).
- Onoda, M., Tatara, G. & Nagaosa, N. Anomalous Hall effect and skyrmion number in real and momentum spaces. *J. Phys. Soc. Jpn.* **73**, 2624–2627 (2004).
- Pugh, E. M. & Rostoker, N. Hall effect in ferromagnetic materials. *Rev. Mod. Phys.* **25**, 151–157 (1953).
- Göbel, B., Mook, A., Henk, J. & Mertig, I. Unconventional topological Hall effect in skyrmion crystals caused by the topology of the lattice. *Phys. Rev. B* **95**, 094413 (2017).
- Cormier, M. et al. Effect of electrical current pulses on domain walls in Pt/Co/Pt nanotracks with out-of-plane anisotropy: spin transfer torque versus joule heating. *Phys. Rev. B* **81**, 024407 (2010).
- Ishizuka, H. & Nagaosa, N. Spin chirality induced skew scattering and anomalous Hall effect in chiral magnets. *Sci. Adv.* **4**, eaap9962 (2018).
- Xu, W. J. et al. Scaling law of anomalous Hall effect in Fe/Cu bilayers. *Eur. Phys. J. B* **65**, 233–237 (2008).

40. Denisov, K. S., Rozhansky, I. V., Averkiev, N. S. & Lähderanta, E. General theory of topological Hall effect in systems with chiral spin textures. *Phys. Rev. B* **98**, 195439 (2018).
41. Zhang, S. Extraordinary Hall effect in magnetic multilayers. *Phys. Rev. B* **51**, 3632 (1995).
42. Hönemann, A., Herschbach, C., Fedorov, D. V., Gradhand, M. & Mertig, I. Insights into spin and charge currents crossing ferromagnetic/nonmagnetic interfaces induced by spin and anomalous Hall effect. Preprint at <https://arxiv.org/abs/1807.06404> (2018).
43. Rajanikant, A., Kasai, S., Ohshima, N. & Hono, K. Spin polarization of currents in Co/Pt multilayer and Co/Pt alloy thin films. *Appl. Phys. Lett.* **97**, 022505 (2010).

Acknowledgements

It is our pleasure to thank A. Petrović for inputs on transport experiments, as well as D. Arovas, A. Auerbach, Shi-Zeng Lin, D. Podolsky, M. Reznikov, and A. Turner for illuminating discussions. We also thank G. Goldman and Y. Schechner for help with image analysis. The work in Singapore was supported by the Ministry of Education (MoE)—Academic Research Fund (Ref. No. MOE2014-T2-1-050), the National Research Foundation—NRF Investigatorship (Reference No. NRF-NRFI2015-04), and the A*STAR Pharos Fund (1527400026). Work at Technion was supported by the Israel Science Foundation (Grant No. 1897/14). We would also like to thank the Micro Nano Fabrication Unit, and to acknowledge support from the Russell Berrie Nano Technology Institute, both at the Technion.

Author contributions

M.R., A.S., O.M.A. and C.P. designed and initiated the research. M.R. deposited the films and characterized them with A.S. and A.K.C.T. M.R. performed and analyzed magnetization and transport measurements with inputs from A.S., O.M.A. and C.P. A.Y. performed the low temperature MFM experiments with assistance from A.A. and A.Y. and O.M.A. analyzed the low temperature MFM data. F.M. performed micromagnetic

simulations and A.Y. analyzed the simulated images. O.M.A. and C.P. coordinated the project. All authors discussed the results and provided inputs to the manuscript.

Additional information

Supplementary Information accompanies this paper at <https://doi.org/10.1038/s41467-018-08041-9>.

Competing interests: The authors declare no competing interests.

Reprints and permission information is available online at <http://npg.nature.com/reprintsandpermissions/>

Journal peer review information: *Nature Communications* thanks the anonymous reviewers for their contribution to the peer review of this work.

Publisher's note: Springer Nature remains neutral with regard to jurisdictional claims in published maps and institutional affiliations.



Open Access This article is licensed under a Creative Commons Attribution 4.0 International License, which permits use, sharing, adaptation, distribution and reproduction in any medium or format, as long as you give appropriate credit to the original author(s) and the source, provide a link to the Creative Commons license, and indicate if changes were made. The images or other third party material in this article are included in the article's Creative Commons license, unless indicated otherwise in a credit line to the material. If material is not included in the article's Creative Commons license and your intended use is not permitted by statutory regulation or exceeds the permitted use, you will need to obtain permission directly from the copyright holder. To view a copy of this license, visit <http://creativecommons.org/licenses/by/4.0/>.

© The Author(s) 2019